https://doi.org/10.3847/2041-8213/ac2600

CrossMark

TOI-3362b: A Proto Hot Jupiter Undergoing High-eccentricity Tidal Migration

Jiayin Dong[1,2], Chelsea X. Huang[3,4], George Zhou[4], Rebekah I. Dawson[1,2], Joseph E. Rodriguez[5], Jason D. Eastman[6], Karen A. Collins[6], Samuel N. Quinn[6], Avi Shporer[3], Amaury H. M. J. Triaud[7], Songhu Wang[8], Thomas Beatty[9], Jonathon M. Jackson[1,2], Kevin I. Collins[10], Lyu Abe[11], Olga Suarez[11], Nicolas Crouzet[12], Djamel Mékarnia[11], Georgina Dransfield[7], Eric L. N. Jensen[13], Chris Stockdale[14], Khalid Barkaoui[15,16], Alexis Heitzmann[4], Duncan J. Wright[4], Brett C. Addison[4], Robert A. Wittenmyer[4], Jack Okumura[4], Brendan P. Bowler[17], Jonathan Horner[4], Stephen R. Kane[18], John Kielkopf[19], Huigen Liu[20], Peter Plavchan[10], Matthew W. Mengel[4], George R. Ricker[3], Roland Vanderspek[3], David W. Latham[6], S. Seager[3,21,22], Joshua N. Winn[23], Jon M. Jenkins[24], Jessie L. Christiansen[25], and Martin Paegert[6]

[1] Department of Astronomy & Astrophysics, 525 Davey Laboratory, The Pennsylvania State University, University Park, PA, 16802, USA; jdong@psu.edu
[2] Center for Exoplanets and Habitable Worlds, 525 Davey Laboratory, The Pennsylvania State University, University Park, PA, 16802, USA
[3] Department of Physics and Kavli Institute for Astrophysics and Space Research, Massachusetts Institute of Technology, Cambridge, MA 02139, USA
[4] University of Southern Queensland, Centre for Astrophysics, West Street, Toowoomba, QLD 4350 Australia
[5] Department of Physics and Astronomy, Michigan State University, East Lansing, MI 48824, USA
[6] Center for Astrophysics | Harvard & Smithsonian, 60 Garden Street, Cambridge, MA 02138, USA
[7] School of Physics & Astronomy, University of Birmingham, Edgbaston, Birmingham B15 2TT, UK
[8] Department of Astronomy, Indiana University, Bloomington, IN 47405, USA
[9] Department of Astronomy and Steward Observatory, University of Arizona, Tucson, AZ 85721, USA
[10] George Mason University, 4400 University Drive MS 3F3, Fairfax, VA, 22030 USA
[11] Université Côte d'Azur, Observatoire de la Côte d'Azur, CNRS, Laboratoire Lagrange, Bd de l'Observatoire, CS 34229, F-06304 Nice cedex 4, France
[12] European Space Agency (ESA), European Space Research and Technology Centre (ESTEC), Keplerlaan 1, 2201 AZ Noordwijk, The Netherlands
[13] Department of Physics & Astronomy, Swarthmore College, Swarthmore, PA 19081, USA
[14] Hazelwood Observatory, Australia
[15] Astrobiology Research Unit, Université de Liége, 19C Allée du 6 Août, B-4000 Liége, Belgium
[16] Oukaimeden Observatory, High Energy Physics and Astrophysics Laboratory, Cadi Ayyad University, Marrakech, Morocco
[17] Department of Astronomy, The University of Texas at Austin, TX 78712, USA
[18] Department of Earth and Planetary Sciences, University of California, Riverside, CA 92521, USA
[19] Department of Physics and Astronomy, University of Louisville, Louisville, KY 40292, USA
[20] School of Astronomy and Space Science, Key Laboratory of Modern Astronomy and Astrophysics in Ministry of Education, Nanjing University, Nanjing 210046, Jiangsu, People's Republic of China
[21] Department of Earth, Atmospheric, and Planetary Sciences, Massachusetts Institute of Technology, Cambridge, MA 02139, USA
[22] Department of Aeronautics and Astronautics, Massachusetts Institute of Technology, Cambridge, MA 02139, USA
[23] Department of Astrophysical Sciences, Princeton University, 4 Ivy Lane, Princeton, NJ 08544, USA
[24] NASA Ames Research Center, Moffett Field, CA 94035, USA
[25] Caltech/IPAC-NASA Exoplanet Science Institute, Pasadena, CA 91125, USA

Abstract

High-eccentricity tidal migration is a possible way for giant planets to be placed in short-period orbits. If this happens often, one would expect to catch proto hot Jupiters on highly elliptical orbits undergoing high-eccentricity tidal migration. As of yet, few such systems have been discovered. Here, we introduce TOI-3362b (TIC-464300749b), an 18.1 day, 5 $M_{\rm Jup}$ planet orbiting a main-sequence F-type star that is likely undergoing high-eccentricity tidal migration. The orbital eccentricity is $0.815^{+0.023}_{-0.032}$. With a semimajor axis of $0.153^{+0.002}_{-0.003}$ au, the planet's orbit is expected to shrink to a final orbital radius of $0.051^{+0.008}_{-0.006}$ au after complete tidal circularization. Several mechanisms could explain the extreme value of the planet's eccentricity, such as planet–planet scattering and secular interactions. Such hypotheses can be tested with follow-up observations of the system, e.g., measuring the stellar obliquity and searching for companions in the system with precise, long-term radial-velocity observations. The variation in the planet's equilibrium temperature as it orbits the host star and the tidal heating at periapse make this planet an intriguing target for atmospheric modeling and observation. Because the planet's orbital period of 18.1 days is near the limit of TESS's period sensitivity, even a few such discoveries suggest that proto hot Jupiters may be quite common.

Unified Astronomy Thesaurus concepts: Exoplanet astronomy (486); Hot Jupiters (753); Transit photometry (1709); Radial velocity (1332); Exoplanet migration (2205)

1. Introduction

High-eccentricity tidal migration has long been proposed to explain the existence of close-in giant planets. In this scenario, a giant planet is formed several au away from its host star. Its orbital eccentricity is excited to a high value, perhaps via planet–planet scattering (e.g., Rasio & Ford 1996; Chatterjee et al. 2008; Nagasawa et al. 2008) or secular interactions, such

as von Zeipel–Lidov–Kozai oscillations (e.g., von Zeipel 1910; Kozai 1962; Lidov 1962; Wu & Murray 2003; see Naoz 2016 for a review) and secular chaos (e.g., Wu & Lithwick 2011). The orbit loses energy due to tidal dissipation as the planet approaches the star near periapse. Once the planet decouples from its perturber, the planet's orbital angular momentum is expected to be conserved (i.e., $L = M_p \sqrt{GM_\star a_p (1 - e_p^2)}$ is

constant). As a consequence, the initially cold planet migrates inward while its orbit circularizes, following the track $a_p(1 - e_p^2) = \text{constant} = a_{\text{final}}$. The final orbital radius of planet a_{final} depends on the planet's initial semimajor axis and eccentricity. The tidal circularization timescale τ_c has a strong dependence on a_{final} (e.g., $\tau_c \propto a_{\text{final}}^8$; Eggleton et al. 1998; Eggleton & Kiseleva-Eggleton 2001; Hansen 2010) and therefore, only cold planets with sufficiently small a_{final} could possibly circularize during the system's lifetime.

If close-in giant planets are products of high-eccentricity tidal migration, we would expect to catch at least some of them on the tidal circularization track (e.g., Socrates et al. 2012). For example, a planet tidally migrating to $a_{\text{final}} = 0.05$ au will have an eccentricity of 0.86 when it is at 0.2 au. As of yet, few close-in giant planets have been observed with such extreme eccentricities and sufficiently small a_{final} (i.e., $a_{\text{final}} \lesssim 0.05$ au; Dawson et al. 2015). HD 80606b ($a_p = 0.46$ au, $e_p = 0.93$; Naef et al. 2001) might be the most impressive example of a proto hot Jupiter undergoing high-eccentricity tidal migration to be a hot Jupiter. The planet's distant stellar companion suggests stellar Kozai cycles as the possible mechanism to excite its extreme eccentricity (Wu & Murray 2003). HAT-P-2b (HD 147506b; $a_p = 0.068$ au, $e_p = 0.52$; Bakos et al. 2007), which has a less extreme eccentricity, could be another example of a proto hot Jupiter undergoing tidal migration and circularization. Long-term radial-velocity observations of the system reveal the presence of a substellar companion (Lewis et al. 2013), also suggesting the stellar Kozai mechanism as the source of the eccentricity excitation. For planets with lower masses, Kepler-1656b ($a_p = 0.20$ au, $e_p = 0.84$, $M_p = 48M_\oplus$; Brady et al. 2018) is an extraordinary example. The high physical density of the planet, along with the extreme eccentricity, might suggest planet–planet interactions such as collision and scattering in the planet's dynamical history.

In this work, we introduce TOI-3362b (TIC-464300749b, 2MASS J10235624-5650353), a transiting proto hot Jupiter that is also likely undergoing high-eccentricity tidal circularization. TOI-3362b was first identified by a systematic search for Warm Jupiters in the Southern Ecliptic Hemisphere in Year 1 of the TESS Full-Frame Images data (Dong et al. 2021). The unusually short duration of the transits compared to the expected duration for a circular orbit (e.g., Dawson & Johnson 2012) pointed to its high eccentricity. Ground-based follow-up observations presented here validate the planet, break the degeneracy between the eccentricity and argument of periapse, and constrain the planet's mass.

In Section 2, we describe the TESS and ground-based photometric and spectroscopic follow-up observations of the target by ASTEP, LCOGT-SSO, CHIRON, and Minerva-Australis. In Section 3, we fit a model to determine the stellar and planetary parameters. In Section 4, we discuss the dynamical implications and propose further investigations of the system.

2. Observations

Here we describe the TESS photometry in Section 2.1, ground-based transit photometry by ASTEP and LCOGT-SSO (Brown et al. 2013) in Section 2.2, and ground-based spectroscopic observations by CHIRON and Minerva-Australis in Section 2.3.

2.1. TESS Photometry

TOI-3362 (TIC-464300749) was observed by TESS with a 30 minute cadence during Sectors 9 and 10 of its primary mission (2019 February 28 to 2019 April 22), and with a 10 minute cadence during Sectors 36 and 37 of its first extended mission (2021 March 07 to 2021 April 28). During a systematic search for warm, large planets using Quick-Look Pipeline lightcurves derived from TESS primary Full-Frame Images (FFIs; Huang et al. 2020a, 2020b; Dong et al. 2021), we detected a candidate transit signal at a period of 18.134 days, with signal-to-pink-noise (i.e., $1/f$ frequency noise) ratio of 22.7. Three transits of TOI-3362b were observed during the TESS primary mission. Preliminary analysis showed that the stellar density ratio $\rho_{\text{circ}}/\rho_\star$, where ρ_{circ} is the inferred stellar density from the lightcurves assuming a circular orbit and $\rho_\star$ is from isochrone fitting, was about 18 (i.e., much larger than 1), and therefore the planetary candidate is highly likely to be on an eccentric orbit (Dong et al. 2014). Here we use early released TESS Image CAlibrator High Level Science Product (HLSP) FFIs (Fausnaugh et al. 2020) in the extended mission to derive the 10 minute cadence lightcurves. The method we employ is similar to that used to derive the standard QLP lightcurves. Three additional transits are observed. We show the raw and detrended lightcurves in Figure 1. The lightcurves are detrended using a Matern-3/2 Gaussian Process (GP) kernel (Foreman-Mackey et al. 2017; Foreman-Mackey 2018). There are no TESS spacecraft events impacting any of the transits. The second transit in the Year 3 data has a relatively high level of noise since it occurred at the beginning of a TESS orbit. We perform the light-curve fit with and without the second transit in Year 3 and find similar planet–star radius ratio posteriors. See Section 3.2 for more details.

2.2. Ground-based Transit Photometry

We used the TESS Transit Finder, which is a customized version of the Tapir software package (Jensen 2013), to schedule our transit observations. We observed three transits as part of the TESS Follow-up Observing Program. The detrended lightcurves from these observations can all be found on the ExoFOP-TESS website.[26]

The Antarctica Search for Transiting ExoPlanets (ASTEP) program observed two transits on the nights of UT 2020 August 10 and UT 2020 August 28 (Guillot et al. 2015; Mékarnia et al. 2016). The 0.4 m telescope is equipped with an FLI Proline science camera with a KAF-16801E, 40964096 front-illuminated CCD and is located on the east Antarctic plateau. The non-filtered red science channel is similar to the R_c band in transmission. The first transit was observed in an $11.\!''2$ aperture including a neighboring star 3.3 magnitude fainter than TOI-3362. The second transit was observed in a $10.\!''1$ aperture. The estimated transit depths from both transits are consistent with the TESS observations.

A full transit of TOI-3362b was observed in the Pan-STARSS z_s and Bessell B band on UT 2021 February 7 using a 1.0 m telescope at the Las Cumbres Observatory Global Telescope (LCOGT; Brown et al. 2013) Siding Spring Observatory (SSO) node in New South Wales, Australia. The LCOGT observations were calibrated with the standard BANZAI pipeline, and the lightcurves were extracted using AstroImageJ (Collins et al. 2017). The observation used an uncontaminated $3.\!''5$ aperture for
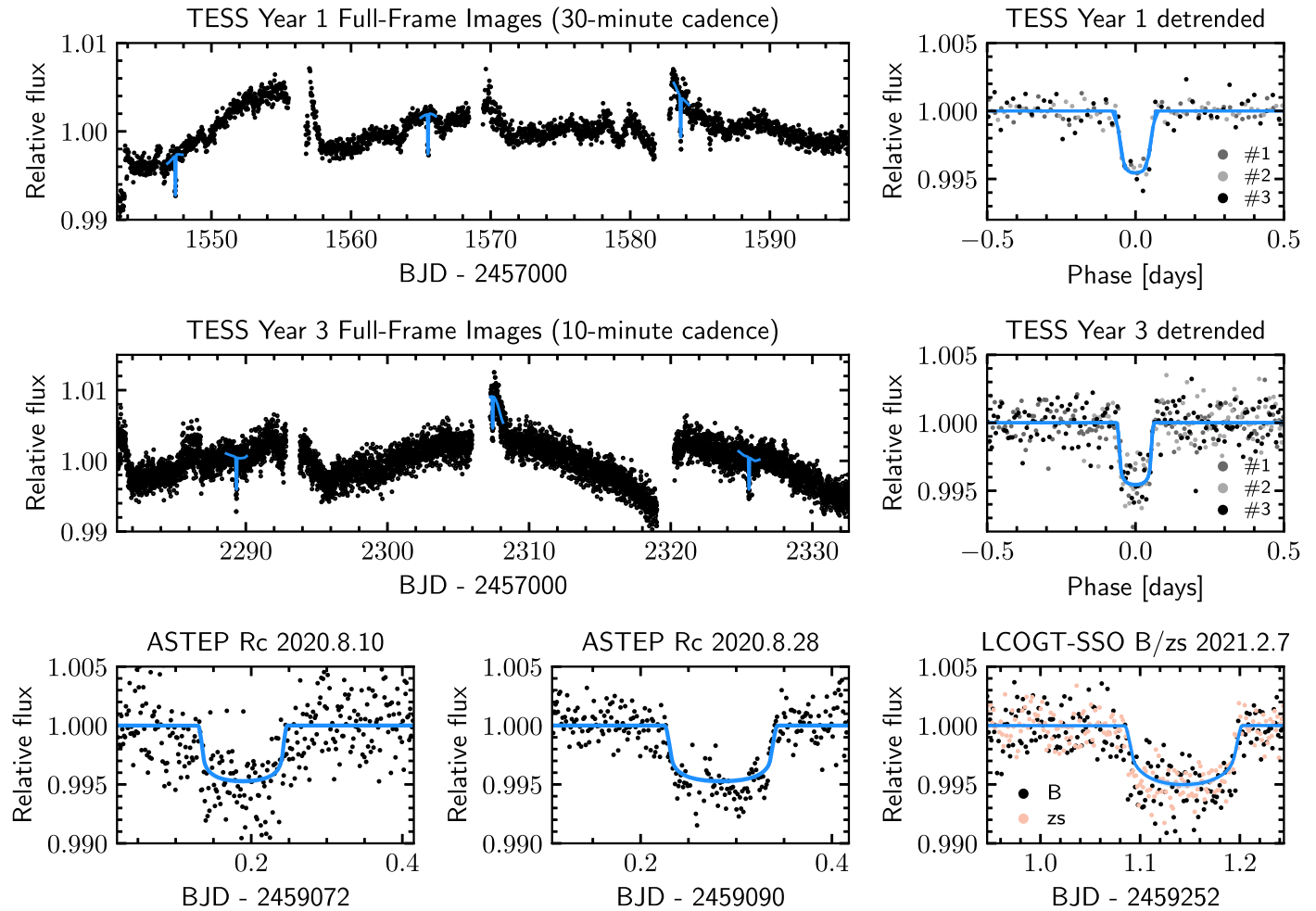

Figure 1. TESS and ground-based transit photometry of TOI-3362b overplotted with best-modeled lightcurves. Both raw (upper and middle left panels) and folded, detrended (upper and middle right panels) TESS Year 1 (30 minutes cadence) and Year 3 (10 minutes cadence) lightcurves are presented. Three detrended, ground-based lightcurves observed with ASTEP and LCOGT-SSO are presented. The LCOGT-SSO transit was detected in two different filters (B and z_s) with no obvious transit depth variation detected.

the z_s and a $4\rlap{.}''67$ aperture for the B band and recovered the expected transit signal. The transit depths from the two bands show no strong chromaticity.

2.3. Spectroscopic Observations

Spectroscopic follow-up observations of TOI-3362 were conducted to measure the orbit and mass of the transiting planet and to refine the atmospheric parameters of the host star. We obtained 21 spectra using the CHIRON echelle spectrograph (Tokovinin et al. 2013) on the SMARTS 1.5 m telescope located at the Cerro Tololo Inter-American Observatory (CTIO), Chile, between UT 2021 April 15 and 2021 May 12. CHIRON is a high-resolution echelle spectrograph fed via an image slicer and a fiber bundle, with a resolving power of $R \approx 80,000$ over the wavelength range of 4100–8700 Å. The wavelength solution is provided via Th-Ar hollow-cathode lamp exposures that were taken after each science exposure. The spectra were extracted via the official CHIRON pipeline (Tokovinin et al. 2013). The radial velocities were derived as per the procedure described in Zhou et al. (2020). Briefly, we derived a line-broadening profile for each spectrum using a least-squares deconvolution (Donati et al. 1997) between the observed spectra and synthetic nonrotating spectral templates generated via the ATLAS9 stellar models (Castelli & Hubrig 2004). The line-broadening profiles were

fit via a convolution of the rotational, macroturbulent, and instrumental broadening kernels, yielding the radial-velocity shift and the rotational broadening velocity. To derive spectroscopic atmospheric parameters for TOI-3362, we match the CHIRON spectra against an observed spectral library that has been classified by the Spectral Classification Pipeline (Buchhave et al. 2012), following the procedure described in Zhou et al. (2020). We measure a spectroscopic effective temperature of $T_{\text{eff}} = 6532^{+88}_{-86}$ K, surface gravity $\log g = 4.072^{+0.032}_{-0.034}$ dex, and bulk metallicity $[\text{M/H}] = 0.017^{+0.057}_{-0.049}$ dex. The star has a stellar type of F5V.

We also obtained nine observations of TOI-3362 between 2021 May 16 and 2021 May 30 using the Minerva-Australis telescope array (Addison et al. 2019), located at Mt. Kent Observatory, Australia. Minerva-Australis is an array of four identical 0.7 m telescopes linked via fiber feeds to a single KiwiSpec echelle spectrograph at a spectral resolving power of $R \approx 80,000$ over the wavelength region of 5000–6300 Å. The array is wholly dedicated to radial-velocity follow-up of TESS planet candidates (e.g., Nielsen et al. 2019; Brahm et al. 2020; Addison et al. 2021). Simultaneous wavelength calibration is provided via two calibration fibers illuminated by a quartz lamp through an iodine cell. The spectra were extracted for each telescope individually and the radial velocities were extracted via the same techniques as

those described above for the CHIRON observations. We note, though, that due to throughput issues, only velocities from Telescope 1 of the MINERVA-Australis array were adopted for this analysis; the remaining telescopes yielded velocity uncertainties too large to contribute meaningfully to the orbit detection.

3. Results

Here we describe models to infer the stellar and planetary parameters. In Section 3.1, we present the stellar isochrone and spectral energy distribution (SED) fitting results. In Section 3.2, we show the transit-only model and report the transit-timing variation analysis and planet's eccentricity inferred purely from lightcurves. In Section 3.4, we describe the transit and radial-velocity joint model and present the planetary parameters.

3.1. Stellar Properties

We used the exoplanet fitting suite EXOFASTv2 (Eastman et al. 2013, 2019) to perform a fit of the SED for TOI-3362. We combined the available Gaia G, B_P, and R_P, (Gaia Collaboration et al. 2018), 2MASS J_{2M}, H_{2M}, and $K_{S,2M}$ (Cutri et al. 2003), and WISE W1 and W2 (Zacharias et al. 2017) photometry with Gaussian priors on the metallicity (0.002 ± 0.070), $T_{\rm eff}$ (6513 ± 100K) from spectroscopy (see Section 2.3), and the Gaia DR2 parallax (2.7265 ± 0.03952 mas, corrected for the $-30\,\mu$as offset reported by Lindegren et al. 2018). We also placed an upper limit on the line-of-sight extinction of 4.1844 mag from Schlegel et al. (1998) and Schlafly & Finkbeiner (2011). Within the fit, the MESA Isochrones and Stellar Tracks (MIST) stellar evolution models (Choi et al. 2016; Dotter 2016) are used to provide better estimates for the host-star parameters. We also put a lower bound on the age of the host star of 100 Myr since we do not see any signs of youth in the photometry or spectroscopy (e.g., from the stellar rotation period and lithium abundance). TIC-464300749 has a mass of $1.445^{+0.069}_{-0.073}\ M_\odot$, a radius of $1.830^{+0.055}_{-0.053}\ R_\odot$, and an age of $2.14^{+0.66}_{-0.52}$ Gyr. See Table 1 for a complete list of the results from this analysis.

We also calculated the stellar density and radius from isochrone fitting with the Dartmouth (Dotter et al. 2008) stellar evolution models. The approach—as described by Dawson et al. (2015)—fits the stellar effective temperature, metallicity, Gaia DR2 parallax, and Gaia apparent g magnitude (Gaia Collaboration et al. 2016, 2018), where the stellar temperature, metallicity, and uncertainties are inferred from the CHIRON spectra. We applied the systematic correction to Gaia parallaxes from Stassun & Torres (2018). The values derived from the Dartmouth model are consistent with the MIST model and have similar uncertainties.

3.2. Transit-only Model

The TESS and ground-based transit photometry have been described in Sections 2.1 and 2.2 and are shown in Figure 1. We only model TESS lightcurves around each transit to roughly six times the transit duration to reduce computational expense. We use a quadratic limb-darkening transit model (Mandel & Agol 2002; Kipping 2013) plus a Matern-3/2 GP kernel with a white-noise term to model the lightcurves (Foreman-Mackey et al. 2017; Foreman-Mackey 2018). We use informative limb-darkening coefficients from Claret (2017) for transits in different filters (TESS, R_c, B, z_s). TESS Year 1 observations, Year 3 observations, and each of the three ground-based observations have their own GP kernels to

account for differences in variability captured by different wavelengths, instruments, and cadences. The stellar density $\rho_{\rm circ}$ is modeled assuming the planet has a circular orbit. We later compare the marginalized $\rho_{\rm circ}$ to $\rho_\star$, the stellar density derived from the isochrone fitting, to constrain the planet's eccentricity. To characterize the transit-timing variation signal of the planet, we model the mid-transit times $T_{1..N}$ individually. All free parameters in the transit-only model are

$$\begin{aligned}
\{ &\rho_{\rm circ}, b, r_p/r_\star, T_{1..N}, \\
&u_{0..1,\rm TESS}, u_{0..1,Rc}, u_{0..1,B}, u_{0..1,z_s}, \\
&s_{\rm TESS,Y1}, \rho_{\rm TESS,Y1}, \sigma_{\rm TESS,Y1} \\
&s_{\rm TESS,Y3}, \rho_{\rm TESS,Y3}, \sigma_{\rm TESS,Y3} \\
&s_{\rm ASTEP,1}, \rho_{\rm ASTEP,1}, \sigma_{\rm ASTEP,1} \\
&s_{\rm ASTEP,2}, \rho_{\rm ASTEP,2}, \sigma_{\rm ASTEP,2} \\
&s_{\rm LCOGT}, \rho_{\rm LCOGT}, \sigma_{\rm LCOGT} \},
\end{aligned} \quad (1)$$

where $\rho_{\rm circ}$ is the stellar density assuming a circular orbit, b is the impact parameter, $r_p/r_\star$ is the planet–star radius ratio, $u_{0..1}$ are the quadratic limb-darkening coefficients, and s is the photometric white noise. The Matern-3/2 GP kernel follows $\mathcal{K}(\tau) = \sigma^2(1 + \sqrt{3}\,\tau/\rho)\exp(-\sqrt{3}\,\tau/\rho)$, where σ represents the amplitude of variability and ρ represents the timescale. The priors used in this model are the same as the ones listed in Table 2 of Dong et al. (2021).

We use the exoplanet package (Foreman-Mackey et al. 2021) for the light-curve fits. Four chains are sampled using the Markov Chain Monte Carlo (MCMC) technique with gradient-based proposals (Hoffman & Gelman 2011; Neal 2012; Betancourt 2017). Each chain contains 50,000 tuning steps and 3000 sampling steps with a target accept rate of 0.95. We assess MCMC convergence using the summary statistics, e.g., Gelman–Rubin diagnostic ($\hat{\mathcal{R}} < 1.1$ for convergence), trace plots, and corner plots (Foreman-Mackey 2016) of the marginal joint distributions. The $\hat{\mathcal{R}}$ values for our model parameters are all less than 1.001 by the end of the sampling. All four chains are combined to get the posteriors.

We use the medians and 1σ uncertainties of the mid-transit time posteriors to perform a least-square fit to a linear line. The orbital period and the conjunction time of the transiting planet are inferred. The $O - C$ residuals, which are calculated by subtracting linear ephemerides from observed mid-transit times, present no significant transit-timing variations. We can rule out any level of transit-timing variability greater than $\sim$5 minutes.

From the stellar density posteriors $\rho_{\rm circ}$ and $\rho_\star$, we infer the eccentricity e and argument of periapse ω of the planet, shown as the black histograms and contours in Figure 2. The stellar densities suggest the planet is on a highly elliptical orbit.

3.3. Transit-only Model with EXOFASTv2

For a consistency check, we also modeled the TESS lightcurve and ground-based transits, along with the stellar model described in Section 3.1 and including planetary eccentricity directly, using EXOFASTv2 (Eastman et al. 2019).

We used keplerspline from Vanderburg & Johnson (2014) to account for the long-term variability of the TESS lightcurves and averaged 10 model data points over the 30 minute Sectors 9 and 10 exposures, and 4 model data points over the 10 minute Sectors 36 and 37 exposures. We also fit a dilution term to the TESS lightcurves to account for poor

Table 1
Median Values and 68% Confidence Intervals for the Stellar and Planetary Parameters of TOI-3362b

Parameter	Units	Values		
Stellar Parameters[a]				
M_*	Mass ($M_\odot$)	$1.445^{+0.069}_{-0.073}$		
R_*	Radius ($R_\odot$)	$1.830^{+0.055}_{-0.053}$		
L_*	Luminosity ($L_\odot$)	$5.48^{+0.37}_{-0.32}$		
ρ_*	Density (cgs)	$0.331^{+0.035}_{-0.032}$		
$\log g$	Surface gravity (cgs)	$4.072^{+0.032}_{-0.034}$		
$T_{\rm eff}$	Effective temperature (K)	6532^{+88}_{-86}		
[M/H]	Bulk metallicity (dex)	$0.017^{+0.057}_{-0.049}$		
$v \sin I_*$	Rotational line broadening (km s^{-1})	20.0 ± 4.1		
Age	Age (Gyr)	$2.14^{+0.66}_{-0.52}$		
EEP	Equal evolutionary phase[b]	369^{+22}_{-19}		
A_V	V-band extinction (mag)	$0.098^{+0.062}_{-0.056}$		
$\sigma_{\rm SED}$	SED photometry error scaling	$0.50^{+0.18}_{-0.11}$		
ϖ	Parallax (mas)	$2.724^{+0.040}_{-0.039}$		
G	Gaia G magnitude	10.705 ± 0.020		
$B_{\rm P}$	Gaia $B_{\rm P}$ magnitude	10.948 ± 0.020		
$R_{\rm P}$	Gaia $R_{\rm P}$ magnitude	10.335 ± 0.020		
J	2MASS J magnitude	9.944 ± 0.024		
H	2MASS H magnitude	9.719 ± 0.022		
$K_{\rm S}$	2MASS $K_{\rm S}$ magnitude	9.693 ± 0.023		
WISE1	WISE1 magnitude	9.651 ± 0.030		
WISE2	WISE2 magnitude	9.678 ± 0.030		
WISE3	WISE3 magnitude	9.643 ± 0.063		
WISE4	WISE4 magnitude	9.427 ± 0.516		
Planetary Parameters (joint model)				
P	Period (days)	$18.09547^{+0.00003}_{-0.00003}$		
T_C	Mid-transit time (BJD-2,457,000)	$1529.325^{+0.001}_{-0.001}$		
b	Transit impact parameter	$0.270^{+0.207}_{-0.184}$		
δ	Transit depth	$0.0041^{+0.0002}_{-0.0002}$		
M_P	Mass ($M_{\rm Jup}$)	$5.029^{+0.668}_{-0.646}$		
R_P	Radius ($R_{\rm Jup}$)	$1.142^{+0.043}_{-0.041}$		
a	Semimajor axis (au)	$0.153^{+0.002}_{-0.003}$		
i	Inclination (°)	$89.140^{+0.584}_{-0.668}$		
e	Eccentricity	$0.815^{+0.023}_{-0.032}$		
ω	Argument of periapse (°)	$50.873^{+11.085}_{-9.165}$		
Instrumental Parameters		u_0	u_1	
$u_{\rm TESS}$	Limb-darkening coefficients	$0.18^{+0.09}_{-0.09}$	$0.30^{+0.10}_{-0.10}$	
$u_{\rm Rc}$	Limb-darkening coefficients	$0.23^{+0.10}_{-0.10}$	$0.39^{+0.10}_{-0.09}$	
u_B	Limb-darkening coefficients	$0.46^{+0.10}_{-0.10}$	$0.30^{+0.10}_{-0.10}$	
$u_{z_{\rm s}}$	Limb-darkening coefficients	$0.13^{+0.10}_{-0.10}$	$0.38^{+0.10}_{-0.10}$	
		s (ppt)	ρ (days)	σ (ppt)
TESS, Y1	Gaussian Process parameters	$0.71^{+0.04}_{-0.04}$	$3.11^{+2.32}_{-1.18}$	$3.83^{+2.27}_{-1.16}$
TESS, Y3	Gaussian Process parameters	$1.25^{+0.04}_{-0.04}$	$2.28^{+1.25}_{-0.71}$	$4.19^{+2.18}_{-1.13}$
ASTEP, 1	Gaussian Process parameters	$5.49^{+0.02}_{-0.01}$	$4.58^{+181.50}_{-4.45}$	$0.59^{+1.23}_{-0.46}$
ASTEP, 2	Gaussian Process parameters	$5.49^{+0.03}_{-0.01}$	$22.80^{+281.40}_{-21.57}$	$2.29^{+4.47}_{-1.15}$
LCOGT	Gaussian Process parameters	$5.50^{+0.03}_{-0.02}$	$2.55^{+155.36}_{-2.53}$	$0.18^{+0.56}_{-0.13}$
		CHIRON	Minerva	
$\gamma_{\rm rel}$	Relative RV offset (m s^{-1})	6450^{+36}_{-37}	7617^{+60}_{-62}	
σ_J	RV jitter (m s^{-1})	3^{+31}_{-3}	5^{+50}_{-5}	
$k_{\rm bkg}$	Radial velocity baseline (m s^{-1}day^{-1})	0^{+4}_{-3}	-1^{+7}_{-7}	

Notes.
[a] The stellar parameters are derived purely from the MIST and SED fitting. See Table 3 in Eastman et al. (2019) for a detailed description of stellar parameters.
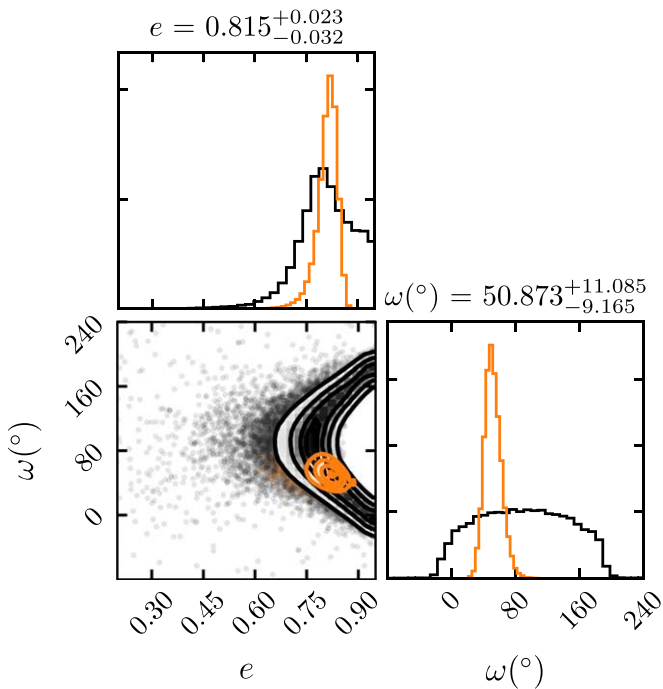[b] Corresponds to static points in a star's evolutionary history; see Section 2 in Dotter (2016).

$$e = 0.815^{+0.023}_{-0.032}$$

$$\omega(°) = 50.873^{+11.085}_{-9.165}$$

Figure 2. Joint posterior distributions of the eccentricity and argument of periapse for TOI-3362b. Values inferred purely from the "photoeccentric" effect are colored in black and from the transit+RV joint fit in orange. The contours are 0.5, 1, 1.5, and 2 sigma levels. Radial-velocity measurements confirm the extreme eccentricity of TOI-3362b and provide much tighter constraints.

background-subtraction (Burt et al. 2020). In practice, fitting the dilution term means the transit depth is defined by the ground-based lightcurves.

The stellar model therefore constrains the stellar density, and the transit duration then constrains the eccentricity.

Most of our values were consistent with the results shown in Section 3.2. In particular, our eccentricity was within 0.05σ. The worst agreement was in our fractional depth which we measured as $R_P/R_* = 0.0685^{+0.0012}_{-0.0010}$—$2.3\sigma$ discrepant, likely because of the different detrending methods.

3.4. Joint Transit and Radial-velocity Modeling

Here we combine the photometry with ground-based spectroscopic observations, as described in Section 2.3, to infer the planet's mass and put a tighter constraint on the eccentricity. Since the planet shows no evidence of transit-timing variations, we directly model its orbital period and conjunction time. The priors of these values follow normal distributions with medians of 18.1 days and 2,458,529.3 BJD, respectively, and uncertainties of 0.1 days.

The joint model has the parameters mentioned in the transit-only model but also includes planet mass M_p, orbital eccentricity e, and argument of periapse ω. Only the stellar density was modeled in the transit-only analysis. To jointly fit the radial-velocity data, we will also need the stellar mass. Picking two parameters out of $\rho_\star$, $M_\star$, and $R_\star$ will be sufficient. We choose $M_\star$ and $R_\star$ for the joint model since the pair shows little covariance in the stellar-fit posteriors discussed in Section 3.1. The stellar-fit posteriors are used as the priors for $M_\star$ and $R_\star$ in the joint model. To account for the instrumentation offsets and systematics, both CHIRON and Minerva-Australis are given an additive offset parameter and a log-normal radial-velocity jitter term. We also include a linear

function of time for both instruments as a baseline model for stellar activity.

We use the exoplanet package for the joint fit, following the same sampling and post-analysis procedures as described in Section 3.2. No significant background trends are found in CHIRON and Minerva-Australis observations. A summary of the posteriors can be found in Table 1. The best-modeled lightcurves and radial-velocity orbit can be found in Figures 1 and 3, respectively.

4. Discussion and Future Work

The inferred semimajor axis and eccentricity of TOI-3362b are consistent with a proto hot Jupiter that is undergoing high-eccentricity tidal migration and will have an orbital radius of $0.051^{+0.008}_{-0.006}$ au (i.e., an orbital period of $3.526^{+0.823}_{-0.584}$ days) after complete tidal circularization (see Section 3.2 of Dawson & Johnson 2018 for a detailed discussion). The timescale for the circularization can be estimated using the equilibrium tide model (Hut 1981), although the estimation has significant uncertainty due to the poorly understood tidal dissipation parameter Q'_p and how it depends on the planet's physical and orbital properties. Neglecting stellar tidal dissipation and assuming that the planet rotates synchronously with its orbit, we adopt Equation (3) in Adams & Laughlin (2006) and find a characteristic circularization timescale of 2.7 Gyr for TOI-3362b, using $Q'_p = 10^6$. We note the estimated timescale could differ by orders of magnitude for different Q'_p assumptions. Moreover, the Q'_p is not a constant during planetary evolution, but has a strong dependence on the planetary radius and semimajor axis. If we instead assume a constant viscous dissipation rate $\bar{\sigma}_p$ (Eggleton et al. 1998; Eggleton & Kiseleva-Eggleton 2001; Hansen 2010) and adopt Equations (2), (3), and (6) in Hansen (2010), we find the circularization timescale to be 4 Gyr, using $\bar{\sigma}_p = 5 \times 10^{-6}$. Again, different assumptions for $\bar{\sigma}_p$ could lead to a very different estimation of the circularization timescale. TOI-3362 has an estimated age of $2.14^{+0.66}_{-0.52}$ Gyr, and is expected to leave the main sequence (MS) and begin its post-MS radial expansion in $\sim$0.5 Gyr according to the MIST model. Comparing the host-star's lifetime to the planet's circularization timescale, it is very plausible that TOI-3362b could not be fully circularized before its host star evolves, even if it acquired its eccentricity early on. If the planet's orbit has not yet been fully circularized, the increasing stellar radiation could inflate the planetary radius and speed up the orbit circularization. After the orbital circularization, the tide raised on the star could introduce stellar dissipation and the orbital decay of the newly formed hot Jupiter. Post-MS evolution of the host star (e.g., stellar radial expansion and mass loss) could introduce orbital instability for TOI-3362b, especially if the system has planetary or stellar companions (e.g., Veras et al. 2013, 2017; Stephan et al. 2018), or lead to engulfment by the host star (e.g., Metzger et al. 2012; Stephan et al. 2020).

In a broad context, in Figure 4, we present the eccentricity versus semimajor axis for all confirmed close-in planets with well-constrained eccentricities (i.e., mass < 13 M_{Jup}, period <365 days) taken from the NASA Exoplanet Archive (DOI 10.26133/NEA12) as of 2021 July 26. The gray region indicates the parameter space in which planets from a large initial semimajor axis could have undergone high-eccentricity tidal migration following the constant angular momentum tracks (i.e., $a_{final} = a(1 - e^2) = $ constant). The upper boundary of the gray region is the limit for avoiding tidal disruption earlier on the migration track. When the initial orbit at the beginning of tidal circularization is highly elliptical, the initial
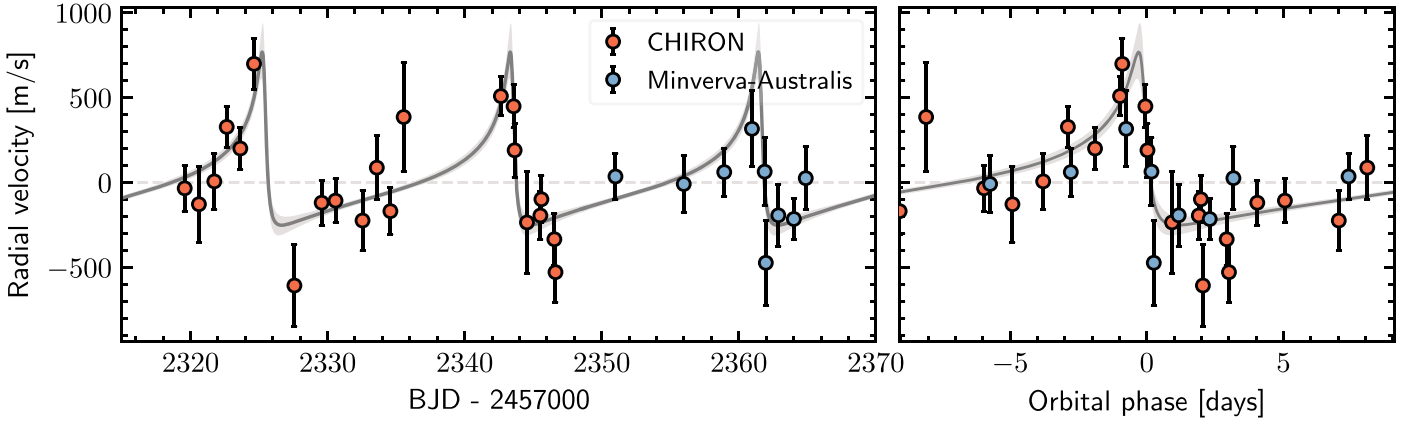
Figure 3. Radial-velocity observations of TOI-3362 by CHIRON colored in orange and Minerva-Australis colored in blue. The instrumental offsets and linear background trends have been abstracted from CHIRON and Minerva-Australis data. The phased radial velocity is plotted in the right panel, where the planet transits at $t = 0$. The median and 1σ uncertainty of the planetary radial-velocity signal are shown in gray.
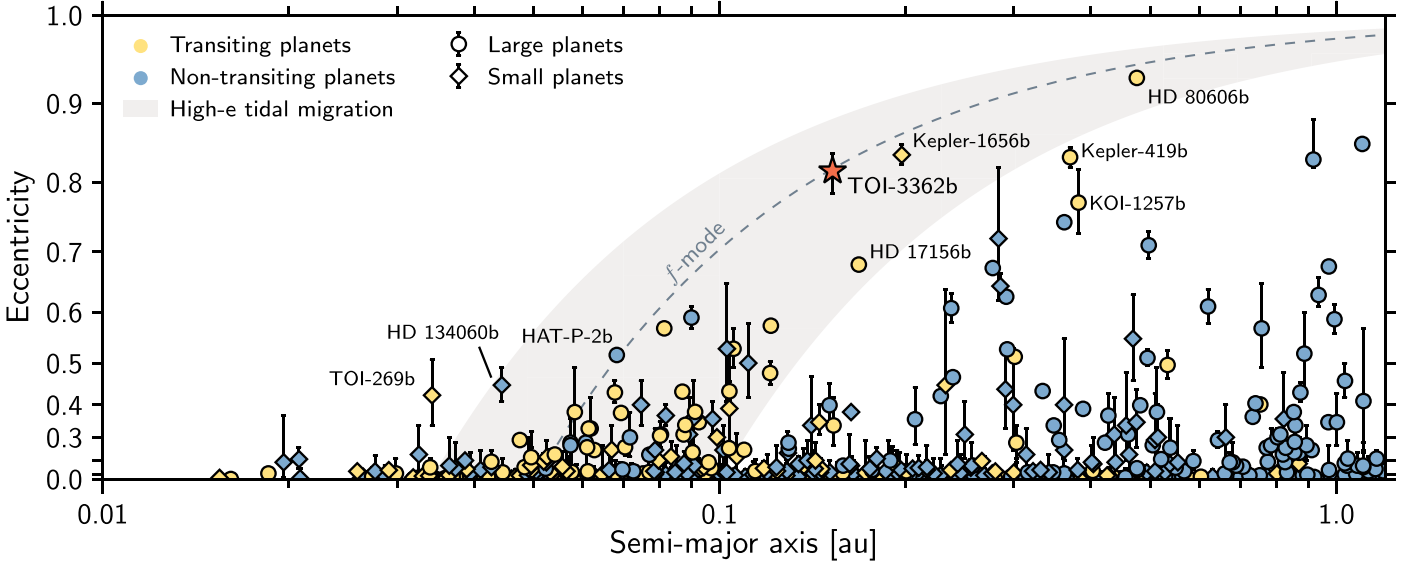

Figure 4. Eccentricity versus semimajor axis for all confirmed planets less than 13 Jupiter-mass with an orbital period less than 365 days. Data are extracted from the NASA Exoplanet Archive (DOI 10.26133/NEA12) as of 2021 July 26. The y-axis is scaled to e^2 to emphasize non-circular planets. The x-axis is in log scale. The gray region with a final semimajor axis range of 0.034–0.1 au is set by the Roche limit and the tidal circularization timescale, respectively. Planets above the dashed gray line could have their f-mode tidal dissipation excited to speed up the migration. Transiting planets are labeled in yellow and non-transiting planets are labeled in blue. Large planets ($R_p > 6R_\oplus$ and/or $M_p > 100M_\oplus$) are labeled as circles and small planets ($R_p < 6R_\oplus$ and/or $M_p < 100M_\oplus$) are labeled as diamonds. To help with the interpretation, we only plot planets with well-constrained eccentricities, which are planets with eccentricity uncertainties less than 50% of the measured eccentricities or uncertainties less than 0.2 for those on nearly circular orbit ($e < 0.2$).

periapse $\approx \frac{1}{2}a_{\text{final}}$ because tracks of constant angular momentum are defined by $a_{\text{final}} = a(1 - e^2)$ and $a(1 - e^2) \approx 2a(1 - e)$ for $e \to 1$. Therefore, only planets with $a_{\text{final}} = 2f_p R_p (M_\star/M_p)^{1/3}$ or greater, where $f_p = 2.7$ (Guillochon et al. 2011), could have avoided tidal disruption during periapse passages. For illustrative purposes, we assume a 1 M_{Jup}, 1.3 R_{Jup} planet orbiting a solar-mass star and derive $a_{\text{final}} = a(1 - e^2) = 0.034$ au, set as the upper boundary of the gray region. The lower boundary of the gray region is set by the tidal circularization timescale. Planets below the region are unlikely to get tidally circularized within their systems' lifetimes. The critical limit for a_{final} depends on the tidal dissipation efficiency, which is not well determined. For illustrative purposes, we adopt the value $a_{\text{final}} = a(1 - e^2) = 0.1$ au, set as the lower boundary of the gray region. For planets that are formed at large semimajor axes and have been undergoing high-eccentricity tidal migration, we would expect to observe them only in the gray

region if they are decoupled from their perturber. We also show the constant angular momentum track for planets with periapses small enough that they could excite planetary f-mode dissipation (Wu 2018; Vick et al. 2019). Above the dashed line, the planet's periapse is close enough to the host star to excite f-mode oscillation which leads to rapid orbital decay from a "cold" Jupiter to a "warm" Jupiter, so we expect an absence of highly elliptical Jupiters (i.e., $e > 0.9$) above that line. We adopt the criterion in Wu (2018), where $a_{\text{final}} = 2f_p R_p (M_\star/M_p)^{1/3}$ and $f_p \approx 4$, and derive $a_{\text{final}} = a(1 - e^2) = 0.05$ au for a 1 M_{Jup}, 1.3 R_{Jup} planet orbiting a solar-mass star.

TOI-3362b stands out because of its extreme eccentricity. Although many giant planets in the semimajor axis range of 0.1–1 au have non-circular orbits, only a few have eccentricities high enough to be consistent with the high-eccentricity tidal migration origin. TOI-3362b joins HD 80606b (Naef et al. 2001;

Wu & Murray 2003) as an example of proto hot Jupiters with an extreme eccentricity, suggesting high-eccentricity tidal migration as one possible origin of hot Jupiters. In Figure 4, we label a few additional interesting systems. The y-axis in Figure 4 is scaled to e^2 to emphasize planets with non-circular orbits. Beside HD 80606b, HAT-P-2b, and Kepler-1656b which have been discussed in Section 1, HD 17156b (Fischer et al. 2007) could undergo tidal migration if its tidal dissipation is efficient enough. Planets below the gray region (e.g., Kepler-419b, Dawson et al. 2014; Jackson et al. 2019; KOI-1257b, Santerne et al. 2014) could periodically reach the migration track if they are coupled to external companions that cyclically excite their eccentricities to higher values.

In Figure 4, we also observe that nearly all the planets to the left of the dashed gray line have been fully circularized, which may indicate that tidal circularization happens very quickly at $a_{final} < 0.05$ au. Two exceptions are TOI-269b (Cointepas et al. 2021) and HD 134060b (Udry et al. 2019), which are both small planets and could have much longer tidal evolution timescales compared to giant planets. For giant planets, the f-mode dissipation could aid the migration during the early stage, e.g., from 1–0.2 au with an eccentricity of 0.98–0.9. Although the f-mode line separates the population, the f-mode dissipation is likely not responsible for the lack of planets with $0.2 < e < 0.9$ since it only works efficiently when the planet has a very large eccentricity.

A group of hot Jupiters on moderately elliptical orbits (i.e., $0.2 < e < 0.6$) are found in the gray region with a_{final} of 0.05–0.1 au, but not many on extremely elliptical orbits. Many of these moderately elliptical planets were discovered with ground-based transit surveys that are not sensitive to longer orbital periods, which might explain why we do not see these moderately eccentric Jupiters' highly eccentric counterparts earlier on the tidal migration track. However, in the Kepler sample—which includes longer orbital periods—Dawson et al. (2015) found a paucity of super-eccentric proto hot Jupiters inconsistent with the prediction of the high-eccentricity tidal migration origin of close-in giant planets (Socrates et al. 2012), assuming a similar share of the Kepler hot Jupiter population has moderately elliptical orbits as the hot Jupiters found in ground-based surveys. Recent work suggests that for planets undergoing the von Zeipel–Lidov–Kozai cycles, their extreme eccentricity spike is very short (e.g., Naoz et al. 2011; Teyssandier et al. 2013) and their transition timescale from cold Jupiters to hot Jupiters is short compared to the timescale the planets spend as cold Jupiters (Petrovich 2015a; Anderson & Lai 2017), making migrating planets hard to detect. A similar short transition timescale is also found in mechanisms such as secular chaos (e.g., Teyssandier et al. 2019) and planet–planet scattering (e.g., Chatterjee et al. 2008; Nagasawa et al. 2008). However, none of these studies could explain the lack of super-eccentric planets ($e > 0.6$) relative to moderately eccentric planets ($0.2 < e < 0.6$; Dawson et al. 2015). One proposed explanation is that planets undergoing tidal migration primarily orbit more metal-rich (i.e., greater than or equal to solar metallicity) stars (Dawson & Murray-Clay 2013), so the Kepler sample lacks both moderately eccentric hot Jupiters and super-eccentric proto hot Jupiters due to the Kepler host stars' overall lower metallicity compared to ground-based surveys (Dawson & Murray-Clay 2013; Guo et al. 2017). TOI-3362 has a metallicity of $[M/H] = 0.017^{+0.057}_{-0.049}$ dex, consistent with the picture of planets undergoing tidal migration, primarily those

orbiting metal-rich stars. We have not computed a formal prediction for the number of super-eccentric Jupiters in the TESS sample, but would have not expected many due to the shorter orbital periods likely to be detected by the TESS mission given the observing strategy. The discovery of TOI-3362b right at the upper limit of TESS planets' most common orbital periods suggests that proto hot Jupiters may not be as rare among bright, nearby stars as they are in the Kepler sample. A final possibility is that hot Jupiters may begin as warm Jupiters instead of cold Jupiters, following in situ formation or disk migration.

Several dynamical processes could explain the extreme eccentricity of TOI-3362b. Generally for Jupiters on the high-eccentricity tidal migration track, the possible dynamical processes include planet–planet scattering (e.g., Rasio & Ford 1996; Chatterjee et al. 2008; Nagasawa et al. 2008), stellar/planetary Kozai cycles with tidal friction (e.g., Wu & Murray 2003; Naoz et al. 2012; Petrovich 2015b) and secular chaos (e.g., Wu & Lithwick 2011). The stellar metallicity trend (Dawson & Murray-Clay 2013) supports mechanisms involving planet–planet interactions (e.g., planet–planet scattering, secular chaos, and planetary Kozai). The short observing baseline and limited radial-velocity precision hinder the detection of radial-velocity accelerations in the TOI-3362 system. From the Gaia EDR3 astrometry (Lindegren et al. 2021), the astrometric noise excess significance is 6.38, which indicates moderate astrometric excess noise. However, the renormalized unit weight error (RUWE) value of TOI-3362 is 0.929, which indicates the excess noise is unlikely to be from orbital motion. The low RUWE value and the fact that Gaia did not report any additional source within 5″ of TOI-3362 can be used to place some limited constraint on the mass of bound companions within 1.5–6.5 au (Penoyre et al. 2020) as well as beyond ∼30 au (Rizzuto et al. 2018; Ziegler et al. 2018). Future Gaia astrometric limits with longer baselines will help to improve such a constraint. Long-term, precise radial-velocity observations will be key to searching for companions in the TOI-3362 system. High-resolution speckle imaging will be helpful to identify or rule out nearby binaries. Excitation of the mutual inclination might also happen during dynamical interactions. The planet is at wide enough separation that it is presumably not realigned by stellar tides. A Rossiter–McLaughlin measurement would, therefore, help to reveal the dynamical history of the planet.

The extreme eccentricity of TOI-3362b makes it an exciting target for atmospheric observations. The incident flux received by TOI-3362b at periapse is ∼80 times higher than the flux it receives at apoapse. The equilibrium temperature at periapse is ∼2500 K, comparable to classic super Hot Jupiters such as WASP-121 (Delrez et al. 2016; Evans et al. 2017). At apoapse, the equilibrium temperature is ∼800 K. As the planet cools down, its atmosphere will cross the equal abundance boundaries of CO/CH_4 and N_2/NH_3 (Fortney et al. 2020). Significant condensation of clouds is also expected due to the dramatic temperature change (Wakeford et al. 2017). TOI-3362b provides an extreme case for studies of dynamic exoplanet atmosphere chemistry. The extreme time varying irradiation would also result in strong super-rotating jets in the atmosphere of TOI-3362b. When observed in relatively long wavelengths near the periapse of the orbit, we expect significant flux change (i.e., Laughlin et al. 2009; Mayorga et al. 2021) and a "ringing" effect due to the planet's rotation (Kataria et al. 2013). These flux variations can be

easily measured by the MIRI instrument on the James Webb Space Telescope and lead to the direct detection of the rotation period of the planet. TOI-3362b may also experience significant tidal heating due to its high eccentricity. Adopting the tidal heating model in Leconte et al. (2010), we estimate the tidal energy dissipation rate is $10^{28}\,\mathrm{erg\,s^{-1}}$, which is 10% of the orbit-averaged irradiation energy the planet receives from the star. Future atmosphere observations exploring the pressure-temperature profile of the planet may reveal the impact of such tidal heating.

Appendix
Radial Velocities for TOI-3362

In Table 2, we present radial-velocity data obtained from the CHIRON and Minerva-Australis spectrographs.

Table 2
Radial Velocities for TOI-3362

BJD	RV (m s^{-1})	σ_{RV} (m s^{-1})	Instrument
2,459,319.576	6423.3	135.8	CHIRON
2,459,320.613	6329.0	224.7	CHIRON
2,459,321.737	6463.0	165.2	CHIRON
2,459,322.642	6783.3	118.6	CHIRON
2,459,323.634	6655.6	123.0	CHIRON
2,459,324.630	7153.7	148.8	CHIRON
2,459,327.580	5846.3	242.0	CHIRON
2,459,329.568	6333.2	132.9	CHIRON
2,459,330.579	6344.9	127.8	CHIRON
2,459,332.550	6226.9	179.4	CHIRON
2,459,333.592	6538.0	190.0	CHIRON
2,459,334.584	6281.0	137.0	CHIRON
2,459,335.551	6835.0	321.0	CHIRON
2,459,342.644	6955.0	114.0	CHIRON
2,459,343.571	6894.5	127.8	CHIRON
2,459,343.648	6635.2	158.0	CHIRON
2,459,344.548	6209.6	299.3	CHIRON
2,459,345.525	6249.9	143.0	CHIRON
2,459,345.601	6345.5	137.8	CHIRON
2,459,346.545	6109.4	152.6	CHIRON
2,459,346.628	5915.4	176.0	CHIRON
2,459,351.004	7667.0	137.0	Minerva-Australis
2,459,355.986	7613.0	170.0	Minerva-Australis
2,459,358.939	7677.0	141.0	Minerva-Australis
2,459,360.963	7928.0	223.0	Minerva-Australis
2,459,361.889	7674.0	199.0	Minerva-Australis
2,459,361.974	7137.0	250.0	Minerva-Australis
2,459,362.885	7415.0	183.0	Minerva-Australis
2,459,364.020	7391.0	123.0	Minerva-Australis
2,459,364.887	7630.0	186.0	Minerva-Australis

ORCID iDs

Jiayin Dong ⓘ https://orcid.org/0000-0002-3610-6953
Chelsea X. Huang ⓘ https://orcid.org/0000-0003-0918-7484
Rebekah I. Dawson ⓘ https://orcid.org/0000-0001-9677-1296
Joseph E. Rodriguez ⓘ https://orcid.org/0000-0001-8812-0565
Jason D. Eastman ⓘ https://orcid.org/0000-0003-3773-5142
Karen A. Collins ⓘ https://orcid.org/0000-0001-6588-9574
Samuel N. Quinn ⓘ https://orcid.org/0000-0002-8964-8377
Avi Shporer ⓘ https://orcid.org/0000-0002-1836-3120
Amaury H. M. J. Triaud ⓘ https://orcid.org/0000-0002-5510-8751
Songhu Wang ⓘ https://orcid.org/0000-0002-7846-6981
Thomas Beatty ⓘ https://orcid.org/0000-0002-9539-4203
Jonathon M. Jackson ⓘ https://orcid.org/0000-0002-0323-4828
Kevin I. Collins ⓘ https://orcid.org/0000-0003-2781-3207
Olga Suarez ⓘ https://orcid.org/0000-0002-3503-3617
Nicolas Crouzet ⓘ https://orcid.org/0000-0001-7866-8738
Djamel Mékarnia ⓘ https://orcid.org/0000-0001-5000-7292
Eric L. N. Jensen ⓘ https://orcid.org/0000-0002-4625-7333
Chris Stockdale ⓘ https://orcid.org/0000-0003-2163-1437
Khalid Barkaoui ⓘ https://orcid.org/0000-0003-1464-9276
Alexis Heitzmann ⓘ https://orcid.org/0000-0002-8091-7526
Duncan J. Wright ⓘ https://orcid.org/0000-0001-7294-5386
Brett C. Addison ⓘ https://orcid.org/0000-0003-3216-0626
Robert A. Wittenmyer ⓘ https://orcid.org/0000-0001-9957-9304
Brendan P. Bowler ⓘ https://orcid.org/0000-0003-2649-2288
Jonathan Horner ⓘ https://orcid.org/0000-0002-1160-7970
Stephen R. Kane ⓘ https://orcid.org/0000-0002-7084-0529
John Kielkopf ⓘ https://orcid.org/0000-0003-0497-2651
Huigen Liu ⓘ https://orcid.org/0000-0001-5162-1753
Peter Plavchan ⓘ https://orcid.org/0000-0002-8864-1667
George R. Ricker ⓘ https://orcid.org/0000-0003-2058-6662
Roland Vanderspek ⓘ https://orcid.org/0000-0001-6763-6562
David W. Latham ⓘ https://orcid.org/0000-0001-9911-7388
Joshua N. Winn ⓘ https://orcid.org/0000-0002-4265-047X
Jon M. Jenkins ⓘ https://orcid.org/0000-0002-4715-9460
Jessie L. Christiansen ⓘ https://orcid.org/0000-0002-8035-4778
Martin Paegert ⓘ https://orcid.org/0000-0001-8120-7457

References

Adams, F. C., & Laughlin, G. 2006, ApJ, 649, 1004
Addison, B., Wright, D. J., Wittenmyer, R. A., et al. 2019, PASP, 131, 115003
Addison, B. C., Wright, D. J., Nicholson, B. A., et al. 2021, MNRAS, 502, 3704
Agol, E., Luger, R., & Foreman-Mackey, D. 2020, AJ, 159, 123
Anderson, K. R., & Lai, D. 2017, MNRAS, 472, 3692
Astropy Collaboration, Price-Whelan, A. M., Sipőcz, B. M., et al. 2018, AJ, 156, 123
Astropy Collaboration, Robitaille, T. P., Tollerud, E. J., et al. 2013, A&A, 558, A33
Bakos, G. Á., Kovács, G., Torres, G., et al. 2007, ApJ, 670, 826
Betancourt, M. 2017, arXiv:1701.02434
Brady, M. T., Petigura, E. A., Knutson, H. A., et al. 2018, AJ, 156, 147
Brahm, R., Nielsen, L. D., Wittenmyer, R. A., et al. 2020, AJ, 160, 235
Brown, T. M., Baliber, N., Bianco, F. B., et al. 2013, PASP, 125, 1031
Buchhave, L. A., Latham, D. W., Johansen, A., et al. 2012, Natur, 486, 375
Burt, J. A., Nielsen, L. D., Quinn, S. N., et al. 2020, AJ, 160, 153
Castelli, F., & Hubrig, S. 2004, A&A, 425, 263
Chatterjee, S., Ford, E. B., Matsumura, S., & Rasio, F. A. 2008, ApJ, 686, 580
Choi, J., Dotter, A., Conroy, C., et al. 2016, ApJ, 823, 102
Claret, A. 2017, A&A, 600, A30
Cointepas, M., Almenara, J. M., Bonfils, X., et al. 2021, A&A, 650, A145
Collins, K. A., Kielkopf, J. F., Stassun, K. G., & Hessman, F. V. 2017, AJ, 153, 77
Cutri, R. M., Skrutskie, M. F., van Dyk, S., et al. 2003, yCat, 2246, 0
Dawson, R. I., & Johnson, J. A. 2012, ApJ, 756, 122
Dawson, R. I., & Johnson, J. A. 2018, ARA&A, 56, 175
Dawson, R. I., Johnson, J. A., Fabrycky, D. C., et al. 2014, ApJ, 791, 89
Dawson, R. I., & Murray-Clay, R. A. 2013, ApJL, 767, L24
Dawson, R. I., Murray-Clay, R. A., & Johnson, J. A. 2015, ApJ, 798, 66
Delrez, L., Santerne, A., Almenara, J. M., et al. 2016, MNRAS, 458, 4025
Donati, J. F., Semel, M., Carter, B. D., Rees, D. E., & Collier Cameron, A. 1997, MNRAS, 291, 658
Dong, J., Huang, C. X., Dawson, R. I., et al. 2021, ApJS, 255, 6
Dong, S., Katz, B., & Socrates, A. 2014, ApJL, 781, L5
Dotter, A. 2016, ApJS, 222, 8
Dotter, A., Chaboyer, B., Jevremović, D., et al. 2008, ApJS, 178, 89
Droettboom, M., Hunter, J., Caswell, T. A., et al. 2016, Matplotlib: Matplotlib V1.5.1, v1.5.1, Zenodo doi: 10.5281/zenodo.44579
Eastman, J., Gaudi, B. S., & Agol, E. 2013, PASP, 125, 83
Eastman, J. D., Rodriguez, J. E., Agol, E., et al. 2019, arXiv:1907.09480
Eggleton, P. P., Kiseleva, L. G., & Hut, P. 1998, ApJ, 499, 853
Eggleton, P. P., & Kiseleva-Eggleton, L. 2001, ApJ, 562, 1012
Evans, T. M., Sing, D. K., Kataria, T., et al. 2017, Natur, 548, 58
Fausnaugh, M. M., Burke, C. J., Ricker, G. R., & Vanderspek, R. 2020, RNAAS, 4, 251
Fischer, D. A., Vogt, S. S., Marcy, G. W., et al. 2007, ApJ, 669, 1336
Foreman-Mackey, D. 2016, JOSS, 1, 24
Foreman-Mackey, D. 2018, RNAAS, 2, 31
Foreman-Mackey, D., Agol, E., Ambikasaran, S., & Angus, R. 2017, AJ, 154, 220
Foreman-Mackey, D., Czekala, I, Luger, R., et al. 2019, dfm/exoplanet: exoplanet v0.2.1, Zenodo, doi:10.5281/zenodo.3462740
Foreman-Mackey, D., Luger, R., Agol, E., et al. 2021, JOSS, 6, 3285
Fortney, J. J., Visscher, C., Marley, M. S., et al. 2020, AJ, 160, 288
Gaia Collaboration, Brown, A. G. A., Vallenari, A., et al. 2018a, A&A, 616, A1

Gaia Collaboration, Prusti, T., de Bruijne, J. H. J., et al. 2016, A&A, 595, A1
Guillochon, J., Ramirez-Ruiz, E., & Lin, D. 2011, ApJ, 732, 74
Guillot, T., Abe, L., Agabi, A., et al. 2015, AN, 336, 638
Guo, X., Johnson, J. A., Mann, A. W., et al. 2017, ApJ, 838, 25
Hansen, B. M. S. 2010, ApJ, 723, 285
Harris, C. R., Jarrod Millman, K., van der Walt, S. J., et al. 2020, arXiv:2006.10256
Hoffman, M. D., & Gelman, A. 2011, arXiv:1111.4246
Huang, C. X., Vanderburg, A., Pál, A., et al. 2020a, RNAAS, 4, 204
Huang, C. X., Vanderburg, A., Pál, A., et al. 2020b, RNAAS, 4, 206
Hunter, J. D. 2007, CSE, 9, 90
Hut, P. 1981, A&A, 99, 126
Jackson, J. M., Dawson, R. I., & Zalesky, J. 2019, AJ, 157, 166
Jensen, E. 2013, Tapir: A web interface for transit/eclipse observability, Astrophysics Source Code Library, ascl:1306.007
Kataria, T., Showman, A. P., Lewis, N. K., et al. 2013, ApJ, 767, 76
Kipping, D. M. 2013, MNRAS, 435, 2152
Kluyver, T., Ragan-Kelley, B., Pérez, F., et al. 2016, in Positioning and Power in Academic Publishing: Players, Agents and Agendas, ed. F. Loizides & B. Scmidt (Amsterdam: IOS Press), 87
Kozai, Y. 1962, AJ, 67, 591
Kumar, R., Carroll, C., Hartikainen, A., & Martin, O. 2019, JOSS, 4, 1143
Laughlin, G., Deming, D., Langton, J., et al. 2009, Natur, 457, 562
Leconte, J., Chabrier, G., Baraffe, I., & Levrard, B. 2010, A&A, 516, A64
Lewis, N. K., Knutson, H. A., Showman, A. P., et al. 2013, ApJ, 766, 95
Lidov, M. L. 1962, P&SS, 9, 719
Lindegren, L., Hernández, J., Bombrun, A., et al. 2018, A&A, 616, A2
Lindegren, L., Klioner, S. A., Hernández, J., et al. 2021, A&A, 649, A2
Luger, R., Agol, E., Foreman-Mackey, D., et al. 2019, AJ, 157, 64
Mandel, K., & Agol, E. 2002, ApJL, 580, L171
Mayorga, L. C., Robinson, T. D., Marley, M. S., May, E. M., & Stevenson, K. B. 2021, arXiv:2105.08009
McKinney, W. 2010, in Proc. of the 9th Python in Science Conf., ed. S. van der Walt & J. Millman (Austin, TX: SciPy), 56
Mékarnia, D., Guillot, T., Rivet, J. P., et al. 2016, MNRAS, 463, 45
Metzger, B. D., Giannios, D., & Spiegel, D. S. 2012, MNRAS, 425, 2778
Naef, D., Latham, D. W., Mayor, M., et al. 2001, A&A, 375, L27
Nagasawa, M., Ida, S., & Bessho, T. 2008, ApJ, 678, 498
Naoz, S. 2016, ARA&A, 54, 441
Naoz, S., Farr, W. M., Lithwick, Y., Rasio, F. A., & Teyssandier, J. 2011, Natur, 473, 187
Naoz, S., Farr, W. M., & Rasio, F. A. 2012, ApJL, 754, L36
Neal, R. M. 2012, arXiv:1206.1901
Nielsen, L. D., Bouchy, F., Turner, O., et al. 2019, A&A, 623, A100
Penoyre, Z., Belokurov, V., Wyn Evans, N., Everall, A., & Koposov, S. E. 2020, MNRAS, 495, 321
Petrovich, C. 2015a, ApJ, 805, 75
Petrovich, C. 2015b, ApJ, 799, 27
Rasio, F. A., & Ford, E. B. 1996, Sci, 274, 954
Rizzuto, A. C., Vanderburg, A., Mann, A. W., et al. 2018, AJ, 156, 195
Salvatier, J., Wiecki, T. V., & Fonnesbeck, C. 2016, PeerJ Computer Science, 2, e55
Santerne, A., Hébrard, G., Deleuil, M., et al. 2014, A&A, 571, A37
Schlafly, E. F., & Finkbeiner, D. P. 2011, ApJ, 737, 103
Schlegel, D. J., Finkbeiner, D. P., & Davis, M. 1998, ApJ, 500, 525
Socrates, A., Katz, B., Dong, S., & Tremaine, S. 2012, ApJ, 750, 106
Stassun, K. G., & Torres, G. 2018, ApJ, 862, 61
Stephan, A. P., Naoz, S., & Gaudi, B. S. 2018, AJ, 156, 128
Stephan, A. P., Naoz, S., Gaudi, B. S., & Salas, J. M. 2020, ApJ, 889, 45
Teyssandier, J., Lai, D., & Vick, M. 2019, MNRAS, 486, 2265
Teyssandier, J., Naoz, S., Lizarraga, I., & Rasio, F. A. 2013, ApJ, 779, 166
Theano Development Team 2016, arXiv:1605.02688
Tokovinin, A., Fischer, D. A., Bonati, M., et al. 2013, PASP, 125, 1336
Udry, S., Dumusque, X., Lovis, C., et al. 2019, A&A, 622, A37
van der Walt, S., Colbert, S. C., & Varoquaux, G. 2011, CSE, 13, 22
Vanderburg, A., & Johnson, J. A. 2014, PASP, 126, 948
Veras, D., Georgakarakos, N., Dobbs-Dixon, I., & Gänsicke, B. T. 2017, MNRAS, 465, 2053
Veras, D., Mustill, A. J., Bonsor, A., & Wyatt, M. C. 2013, MNRAS, 431, 1686
Vick, M., Lai, D., & Anderson, K. R. 2019, MNRAS, 484, 5645
Virtanen, P., Gommers, R., Oliphant, T. E., et al. 2020, NatMe, 17, 261
von Zeipel, H. 1910, AN, 183, 345
Wakeford, H. R., Visscher, C., Lewis, N. K., et al. 2017, MNRAS, 464, 4247
Wu, Y. 2018, AJ, 155, 118
Wu, Y., & Lithwick, Y. 2011, ApJ, 735, 109
Wu, Y., & Murray, N. 2003, ApJ, 589, 605
Zacharias, N., Finch, C., & Frouard, J. 2017, yCat, 1340
Zhou, G., Winn, J. N., Newton, E. R., et al. 2020, ApJL, 892, L21
Ziegler, C., Law, N. M., Baranec, C., et al. 2018, AJ, 156, 259